

Ion dynamics and CO₂ absorption properties of Nb, Ta and Y-doped Li₂ZrO₃ studied by solid-state NMR, thermogravimetry and first-principles calculations

Matthew T. Dunstan,[†] Hannah Laeverenz Schlogelhofer,[†] John M. Griffin,[‡]
Matthew S. Dyer,[¶] Michael W. Gaultois,[†] Cindy Y. Lau,[§] Stuart A. Scott,[§] and
Clare P. Grey^{*,†}

Department of Chemistry, University of Cambridge, Lensfield Road, Cambridge, CB2 1EW, United Kingdom, Department of Chemistry, Lancaster University, Lancaster LA1 4YB, United Kingdom, Department of Chemistry, University of Liverpool, Crown Street, Liverpool L69 7ZD, United Kingdom, and Department of Engineering, University of Cambridge, Trumpington Street, Cambridge, CB2 1PZ, United Kingdom

E-mail: cpg27@cam.ac.uk

Abstract

Amongst the many different processes proposed for large scale carbon capture and storage (CCS), high temperature CO₂ looping has emerged as a favourable candidate due to the low theoretical energy penalties that can be achieved. Many different materials have been proposed for use in such a process, the process requiring fast CO₂ absorption reaction kinetics, as

*To whom correspondence should be addressed

[†]Department of Chemistry, University of Cambridge, Lensfield Road, Cambridge, CB2 1EW, United Kingdom

[‡]Department of Chemistry, Lancaster University, Lancaster LA1 4YB, United Kingdom

[¶]Department of Chemistry, University of Liverpool, Crown Street, Liverpool L69 7ZD, United Kingdom

[§]Department of Engineering, University of Cambridge, Trumpington Street, Cambridge, CB2 1PZ, United Kingdom

well as being able to cycle the material for multiple cycles without loss of capacity. Lithium ternary oxide materials, and in particular Li_2ZrO_3 , have displayed promising performance but further modifications are needed to improve their rate of reaction with CO_2 . Previous studies have linked rates of lithium ionic conduction with CO_2 absorption in similar materials, and in this work we present work aimed at exploring the effect of aliovalent doping on the efficacy of Li_2ZrO_3 as a CO_2 sorbent. Using a combination of x-ray powder diffraction, theoretical calculations and solid-state nuclear magnetic resonance, we studied the impact of Nb, Ta and Y doping on the structure, Li ionic motion and CO_2 absorption properties of Li_2ZrO_3 . These methods allowed us to characterise the theoretical and experimental doping limit into the pure material, suggesting that vacancies formed upon doping are not fully disordered, but instead are correlated to the dopant atom positions, limiting the solubility range. Characterisation of the lithium motion using variable temperature solid-state nuclear magnetic resonance confirms that interstitial doping with Y retards the movement of Li ions in the structure, whereas vacancy doping with Nb or Ta **results in a similar activation as Li_2ZrO_3** . However, a marked reduction in the CO_2 absorption of the Nb and Ta doped samples suggests that doping also leads to a change in the carbonation equilibrium of Li_2ZrO_3 disfavouring the CO_2 absorption at the reaction temperature. This study shows that a complex mixture of structural, kinetic and dynamic factors can influence the performance of Li-based materials for CCS, and underscores the importance of balancing these different factors in order to optimise the process.

Introduction

The ambitious targets set by governments around the world to reduce levels of greenhouse emissions require the implementation of new technologies to simultaneously decarbonise the economy while at the same time maintaining the economic output and growth that is expected to continue. Many different technologies have been proposed to help reduce the amount of CO_2 emissions from various parts of the economy, in particular from the power production sector, with varying levels of cost effectiveness and readiness. Carbon capture and storage (CCS) methods are going to be a nec-

essary part of the mix of technologies used to meet these emissions targets, and their improvement and implementation is the focus of much current research.¹

The use of current mature CCS technologies such as liquid amines imposes a very large energy penalty (~8-12.5%) to their associated power plants, in addition to problems with corrosion and degradation caused by the hazardous solvents.^{2,3} This reduction in generation efficiency leads to higher electricity prices, and as such it is desirable to develop new technologies with lower energy penalties so as to be able to implement CCS on a much wider scale, with only a few full-scale reactors currently being used.

A promising new approach involves the reversible reaction of CO₂ with various alkali oxide materials at elevated temperatures, resulting in the separation of CO₂ from the flue gas, ready for storage. The process is generally known as high temperature CO₂ absorption looping, as the material involved can be looped between its carbonated and regenerated states many times to perform an efficient separation. The most studied system is CaO-CaCO₃, which has a projected energy penalty of 6-8%, representing a marked improvement over other currently used processes.^{2,4} This is in part due to the fact that this process operates at very high temperatures (923–1223 K), which allows for the reintegration of waste heat back into the power generation cycle. However, the CaO-CaCO₃ system suffers from capacity fading after cycling for a long period of time, making it necessary to constantly inject new material into the CO₂ looping process.⁵

Many oxides of alkali and alkali earth metals including Li₂O,⁶ MgO,⁷ Li₂ZrO₃,^{8,9} Li₆Zr₂O₇,¹⁰ Li₄SiO₄,¹¹ Li₅AlO₄,¹² have been shown to be potential candidates for intermediate and high temperature CO₂ sorbents, and to be capable of reversibly reacting with CO₂ at elevated temperatures. Importantly, these materials have been shown to achieve stable capacities upon repeated cycling, offering a more materials-cost efficient alternative to CaO for CO₂ looping.

After CaO, Li₂ZrO₃ was the first material to be studied intensively that undergoes reversible carbonation:⁸



The reaction is exothermic, and generally occurs at lower temperatures than the CaO-CaCO₃ system (673–873 K), an advantage that would lead to lower energy penalties for use in CCS. However, subsequent studies showed that the very slow kinetics of the carbonation reaction would limit its use in a cyclic process.¹³ A double shell model for the carbonation of Li₂ZrO₃ was proposed by Ida *et al.*, in which the initial rapid reaction of CO₂ with Li₂ZrO₃ first forms an outer layer of Li₂CO₃ around a layer of ZrO₂ covering a core of unreacted Li₂ZrO₃.¹⁴ After this initial absorption process, carbonation can continue, but requires the motion of Li⁺ and O²⁻ ions through the ZrO₂ and Li₂CO₃ layers or through the grain boundaries, leading to a kinetically limited reaction rate.

Our previous research in this area has sought to directly measure the rate of ionic motion in CCS materials in order to understand its connection with the observed carbonation reaction behaviour better. Nuclear magnetic resonance (NMR) is well suited to such an analysis, being able to directly probe a **nucleus** of interest for both its local structural environment via the chemical shift, as well as quadrupolar interactions for some nuclei (including ⁷Li and ¹⁷O), making it possible to access information about rates of atomic and ionic motion over a wide range of timescales between $\sim 10^3 - 10^7$ s⁻¹. A combined ⁷Li and ¹⁷O variable temperature NMR study on Li₂CO₃¹⁵ (a common component in all Li-based CO₂ looping systems) found a correlation between increased rates of Li ionic motion at higher temperatures and increased rates of CO₃²⁻ rotation, with these increases in ionic mobility occurring over the same temperature range as the marked increase in carbonation kinetics of materials such as Li₅AlO₄ and Li₂CuO₂.¹⁶⁻¹⁸ Indeed, similar NMR experiments have recently been performed on Li₂ZrO₃ to determine the activation energy and mechanism for Li ionic conduction, finding that above 500 K there is an abrupt thermally activated diffusion of Li ions through the structure with an activation energy of ~ 0.64 eV.¹⁹

Given the importance of ionic conductivity on the behaviour of these materials, new chemical modifications that seek to modify a materials' rate of diffusion could lead to associated changes in its CO₂ absorption properties. A common modification involves the mixing of Li₂ZrO₃ with other materials such as K₂CO₃ or Na₂CO₃ in the hope of improving reaction rates. The addition of

K_2CO_3 has been shown to lead to faster carbonation rates as compared to undoped Li_2ZrO_3 ,^{9,20–22} potassium and lithium forming a eutectic molten carbonate on the surface of sorbent particles which is proposed to aid lithium and oxygen ion conduction.²³ The addition of Na to form mixtures of Li_2ZrO_3 and Na_2ZrO_3 also created sorbents with improved reaction kinetics,^{24,25} with absorption rates approximately twenty times faster for 5 % doped Li_2ZrO_3 .²⁶

Kato *et al.* in their comparative studies of the CO_2 absorption properties of Li_2ZrO_3 and Li_4SiO_4 , expanded upon the connection between ionic conduction and absorption kinetics.²⁷ A reason put forward to explain the observed superior CO_2 absorption properties of Li_4SiO_4 over Li_2ZrO_3 , the former being able to absorb CO_2 faster at lower partial pressures and lower temperatures, is the improved Li^+ mobility due to more available sites for lithium-hopping. There are six crystallographically distinct Li sites in ordered Li_4SiO_4 , each with partial occupancy factors between $\frac{1}{3}$ and $\frac{2}{3}$, and taken together they form a continuous network constructed from edge and corner sharing LiO_4 , LiO_5 and LiO_6 polyhedra.²⁸ Consistent with this analysis, introducing Li vacancies through doping with P or S or Li interstitials with Al greatly improves the ionic conductivity of Li_4SiO_4 through activation of these lithium ion conduction pathways.²⁹

Despite many studies on hetero, non-alkali doping in Li_4SiO_4 , to our knowledge no similar studies have been carried out on Li_2ZrO_3 . In this work we present experimental studies into the influence of Nb, Ta and Y doping on the ionic conduction and CO_2 absorption properties of Li_2ZrO_3 using both **variable-temperature** (VT) NMR and TGA methods. Doping Zr with 5+ atoms such as Nb and Ta is expected to lead to the formation of Li ion vacancies, whereas doping with 3+ atoms such as Y is expected to lead to the formation of Li interstitials, allowing the comparison of the influence of these two different modifications. Through the analysis of the NMR data we were able to determine the activation energy of Li ion diffusion in these doped materials and compare it to the undoped material as reported in Baklanova *et al.*,¹⁹ before considering these results in the context of the observed CO_2 absorption behaviour of these doped materials. This work explores the influence of doping on both ionic conduction and CO_2 absorption, allowing deeper insights to be gained into the underlying mechanism of CO_2 absorption by mixed lithium oxides.

Experimental Methods

Synthesis and characterisation

Samples in the solid-solution series $\text{Li}_{2-x}\text{Zr}_{1-x}\text{Nb}_x\text{O}_3$ and $\text{Li}_{2-x}\text{Zr}_{1-x}\text{Ta}_x\text{O}_3$ ($x = 0.05, 0.10, 0.25$) were prepared from Li_2CO_3 (Sigma Aldrich, 99.997%), ZrO_2 (Alfa Aesar, 99%), Nb_2O_5 (Sigma Aldrich, 99.9%) and Ta_2O_5 (Sigma Aldrich, 99%), while $\text{Li}_{2+x}\text{Zr}_{1-x}\text{Y}_x\text{O}_3$ ($x = 0.05, 0.10$) samples were prepared from Li_2CO_3 , ZrO_2 and Y_2O_3 (Alfa Aesar, 99.999%). Stoichiometric quantities of the starting materials were weighed out and ground in an agate mortar and pestle with EtOH. The samples were then placed in alumina crucibles and calcined for 12 hours at 873 K and then for two periods of 12 hours at 1173 K, with regrinding between each step. The $\text{Li}_{2-x}\text{Zr}_{1-x}\text{Nb}_x\text{O}_3$ and $\text{Li}_{2-x}\text{Zr}_{1-x}\text{Ta}_x\text{O}_3$ samples were further calcined for another 12 hours at 1273 K. To ensure sample purity, room-temperature X-ray powder diffraction (XRD) data were collected on a Panalytical X'Pert Pro diffractometer using $\text{Cu K}\alpha$ radiation.

Secondary and backscattered electron micrographs were collected using a field emission gun scanning electron microscope (Camscan MX2600) operating at an accelerating voltage of 25 kV. 20 nm of Pd was sputter-deposited on specimens to minimize charging. Energy dispersive X-ray (EDX) spectra were collected using an Oxford Instruments Inca x-act detector. The sample area investigated at 25 kV in LiZrO_3 is estimated to be $\sim 150 \mu\text{m}^2$. Multiple areas across 3 particles were examined to confirm the homogeneous distribution of substituted elements.

Theoretical calculations

The energetic cost of forming Li vacancies in Li_2ZrO_3 by replacing Zr^{4+} with Nb^{5+} or Ta^{5+} was assessed using plane-wave based density functional theory (DFT). One of the four crystallographically equivalent Zr^{4+} ions within the experimental unit cell of Li_2ZrO_3 ³⁰ was replaced with the Nb^{5+} and Ta^{5+} ion, and SimDope.py³¹ was then used to generate the eight symmetrically unique cells generated by placing Li vacancies at one of the two crystallographically distinct Li sites within the unit cell. The resulting cells have a composition of $\text{Li}_7\text{Zr}_3(\text{Nb,Ta})\text{O}_{12}$, equivalent to

$\text{Li}_{2-x}\text{Zr}_{1-x}(\text{Nb,Ta})_x\text{O}_3$ ($x = 0.25$). Further calculations were performed in a $2 \times 2 \times 2$ supercell, substituting one Zr for Ta, equivalent to $\text{Li}_{2-x}\text{Zr}_{1-x}\text{Ta}_x\text{O}_3$ ($x = 1/32$), giving 40 symmetrically unique cells. The atomic positions and cell parameters were optimised for every doping configuration until all atomic forces were below 0.01 eV/\AA .

All DFT calculations were performed using the VASP code,³² with the PBE functional³³ and using the projector augmented wave method³⁴ to treat core electrons. A plane-wave cutoff of 600 eV was used, along with a $5 \times 3 \times 5$ k-point grid for the Li_2ZrO_3 sized cells, and a $3 \times 2 \times 3$ k-point grid in the larger supercells.

The stability of the lowest energy doped cell at 0 K was assessed by comparing the energy of the cell to that of the convex hull of experimentally reported $\text{Li}^+ \text{-Zr}^{4+} \text{-(Nb,Ta)}^{5+} \text{-O}^{2-}$ phases: Li_2O , ZrO_2 , Li_2ZrO_3 , Nb_2O_5 , LiNbO_3 , Li_3NbO_4 , Ta_2O_5 , LiTaO_3 , and Li_3TaO_4 . The structures of these phases were taken from the ICSD,³⁵ and their energies obtained following a full cell and structure optimisation using equivalent DFT parameters to those described above. Convex hulls were constructed using the pymatgen software.³⁶

Finite temperature effects were included by calculating the mixing entropy, ΔS_{mix}^1 , of the doped phase, $\text{Li}_{2-x}\text{Zr}_{1-x}(\text{Nb,Ta})_x\text{O}_3$, assuming disorder of the $(1-x)$ Zr^{4+} and x $\text{Nb}^{5+}/\text{Ta}^{5+}$ ions on the same crystallographic site, and treating the Li^+ ions and vacancies as being similarly disordered with $(1-x/2)$ Li^+ ions and $x/2$ vacancies on each of the two crystallographic Li sites in Li_2ZrO_3 . In this case,

$$\Delta S_{mix}^1 = k_B x \ln(x) + (1-x) \ln(1-x) + 2[(x/2) \ln(x/2) + (1-x/2) \ln(1-x/2)]. \quad (2)$$

An alternative mixing entropy, ΔS_{mix}^2 , was calculated assuming that the Li vacancy was always located adjacent to the dopant atom, such that only the contribution from Zr^{4+} and $\text{Nb}^{5+}/\text{Ta}^{5+}$ ions was included:

$$\Delta S_{mix}^2 = k_B x \ln(x) + (1-x) \ln(1-x). \quad (3)$$

The doping free energy, ΔF_{dope}^n , was then calculated as $\Delta F_{dope}^n = x\Delta H_{dope} - T\Delta S_{mix}^n$, where ΔH_{dope} is the previously calculated height of the doped system above the convex hull at a concentration of $x = 0.25$.

Nuclear Magnetic Resonance

^7Li NMR spectra were obtained at 9.4 T on a Bruker Avance 400 MHz spectrometer operating at a Larmor frequency of 155.46 MHz. Variable temperature measurements from room temperature to 771 K were performed using a Bruker laser probe.^{37,38} Temperature calibration of the probe was carefully performed by using the ^{79}Br resonance of KBr ³⁹ over the whole temperature range. The temperatures given in the text correspond to actual sample temperatures with an estimated accuracy of ± 10 , 20 and 30 K in the 293–473 K, 473–673 K and 673–771 K temperature ranges. Samples were packed in 4 mm BN inserts within 7 mm zirconia rotors, which were subsequently spun at 4 kHz. One-dimensional experiments were performed with a rotor-synchronised spin-echo pulse sequence with a 1.33 μs excitation pulse. Relaxation experiments were performed with a saturation recovery pulse sequence. The ^7Li chemical shifts were externally referenced to 1 M LiCl in H_2O at 0 ppm.

Thermogravimetry

The carbonation behaviour of the samples was investigated using a thermogravimetric analyser (TGA/DSC 1, Mettler Toledo) operating at atmospheric pressure, as described in our previous studies of CCS materials.⁴⁰ In each experiment, a sample of ~ 20 mg of powder was placed in a 70 μL alumina crucible, supported on a cantilever-type balance. Gases were fed to the reaction chamber through three gas ports, *viz.* reactive gas, purge gas and protective gas. The reaction chamber was electrically heated by a tubular furnace surrounding the balance. Both the protective gas and the purge gas were N_2 , and were fed to the TGA reaction chamber with a flow rate of 50 mL min^{-1} . The reactive gas was a stream of pre-mixed N_2 and CO_2 , fed by a capillary so that the gas could flow over the top of the crucible. The partial pressure of CO_2 at the surface of the

solid sample was adjusted by varying the mix of N₂ and CO₂ in the reactive gas, while keeping a constant overall flow rate of 50 mL min⁻¹.

The actual CO₂ concentration at the gas-solid interface was calibrated against the well-understood thermodynamic CaO/CaCO₃ carbonation equilibrium.⁴¹ For example, when a carbonated sample of pure CaO (98 wt %) was slowly heated in a specific mixture of CO₂ and N₂, the temperature at the onset of CaCO₃ decomposition was recorded and the corresponding CO₂ partial pressure in contact with the solid phase was determined from the phase diagram of the CaO-CaCO₃-CO₂ system. In the carbonation experiments, the samples were heated from 373 K to either 873 K or 973 K under a specific partial pressure of CO₂, i.e. a specific N₂/CO₂ ratio, while the calcination experiments were carried out at 1273 K under N₂.

Results

Powder X-ray Diffraction

The x-ray diffraction patterns of Li_{2-x}Zr_{1-x}Nb_xO₃ and Li_{2-x}Zr_{1-x}Ta_xO₃ for $x = 0, 0.05, 0.1, 0.25$ and 0.5 are shown in Figure 1. In the case of both systems, even at the smallest dopant level of $x = 0.05$, peaks corresponding to impurity phases of Li₃NbO₄⁴² or Li₃TaO₄⁴³ and ZrO₂⁴⁴ can be observed in addition to the peaks from the known monoclinic Li₂ZrO₃ structure.³⁰

As the level of Nb doping increases, a shift in the position of the reflections of the Li₂ZrO₃ to higher angles indicates a reduction in lattice parameters consistent with the substitution of the smaller Nb or Ta atom for Zr, the atomic radii decreasing from 0.72 Å for Zr to 0.64 Å for Nb and Ta.⁴⁵ This shows that while the addition of Nb or Ta leads to the formation of impurity phases, there is nevertheless some incorporation into Li₂ZrO₃. SEM-EDX analysis of Li_{1.95}Zr_{0.95}Nb_{0.05}O₃ confirms this observation, as X-ray fluorescence of both Nb and Zr are seen in individual particles (see Supporting Information).

To obtain more accurate information as to the amount of Zr substitution for Nb or Ta, we performed Rietveld refinements on the data using GSAS with the graphical interface EXPGUI.^{46,47}

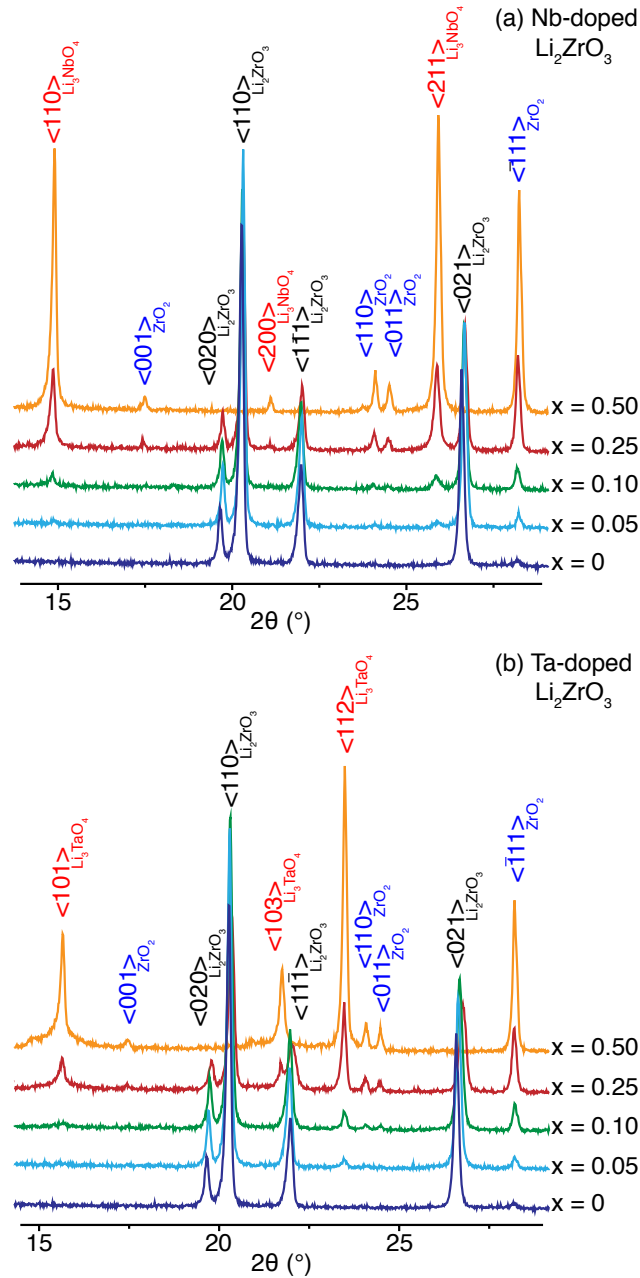
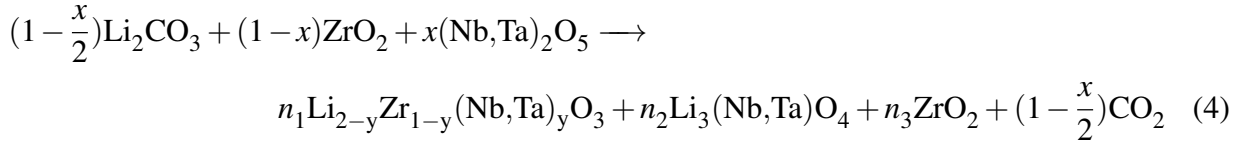


Figure 1: X-ray diffractograms ($\lambda = 1.54056 \text{ \AA}$) of (a) $\text{Li}_{2-x}\text{Zr}_{1-x}\text{Nb}_x\text{O}_3$ and (b) $\text{Li}_{2-x}\text{Zr}_{1-x}\text{Ta}_x\text{O}_3$, with $x = 0, 0.05, 0.1, 0.25$ and 0.5 . Reflections corresponding to the different phases presents are marked. Even at the lowest doping levels impurity phases of Li_3NbO_4 , Li_3TaO_4 and ZrO_2 can be seen, indicating a low solubility limit of Nb and Ta into Li_2ZrO_3 .

A sample multiple phase refinement for the sample with nominal composition $\text{Li}_{1.75}\text{Zr}_{0.75}\text{Nb}_{0.25}\text{O}_3$ is shown in Figure 2. From the refinements it was also possible to extract phase fractions for the different phases present, labelled n_1 , n_2 and n_3 corresponding to the synthesis reaction:



This allows us to relate the nominal amount of doping, x , with the actual amount of doping, y , by using the refined phase fractions in the following equation:

$$y = \frac{x - n_2}{n_1} \quad (5)$$

The refined phase fractions for the different nominal amounts of Nb and Ta doping, along with the derived actual dopant concentrations, are shown in Table 1. From these results it can be seen that despite the presence of small amounts of impurities, the members of the solid solution correspond well (within error) to their nominal composition. The exception to this is the $\text{Li}_{1.75}\text{Zr}_{0.75}\text{Ta}_{0.25}\text{O}_3$ sample, with a derived dopant concentration of $x \approx 0.35$ compared to the nominal $x = 0.25$. A possible source of this error is the extent of peak overlap between the Li_2ZrO_3 and Li_3TaO_4 phases in the sample, leading to inaccuracies in the refined phase fractions.

Table 1: Rietveld-refined phase fractions and calculated value of dopant, y , for the Nb and Ta doping of Li_2ZrO_3 .

Dopant M	Nominal doping x	Phase Fractions			Actual doping y
		$\text{Li}_{2-y}\text{Zr}_{1-y}\text{M}_y\text{O}_3, n_1$	$\text{Li}_3\text{MO}_4, n_2$	ZrO_2, n_3	
Nb	0.00	0.908 ± 0.001	0	0.092 ± 0.001	0
	0.05	0.896 ± 0.002	0.002 ± 0.001	0.102 ± 0.002	0.054 ± 0.003
	0.10	0.873 ± 0.001	0.022 ± 0.003	0.105 ± 0.006	0.089 ± 0.012
	0.25	0.553 ± 0.007	0.123 ± 0.004	0.324 ± 0.004	0.230 ± 0.008
Ta	0.00	0.908 ± 0.001	0	0.092 ± 0.001	0
	0.05	0.910 ± 0.002	0.006 ± 0.003	0.084 ± 0.009	0.048 ± 0.002
	0.10	0.899 ± 0.005	0.012 ± 0.002	0.090 ± 0.003	0.098 ± 0.002
	0.25	0.531 ± 0.002	0.063 ± 0.003	0.405 ± 0.006	0.351 ± 0.003

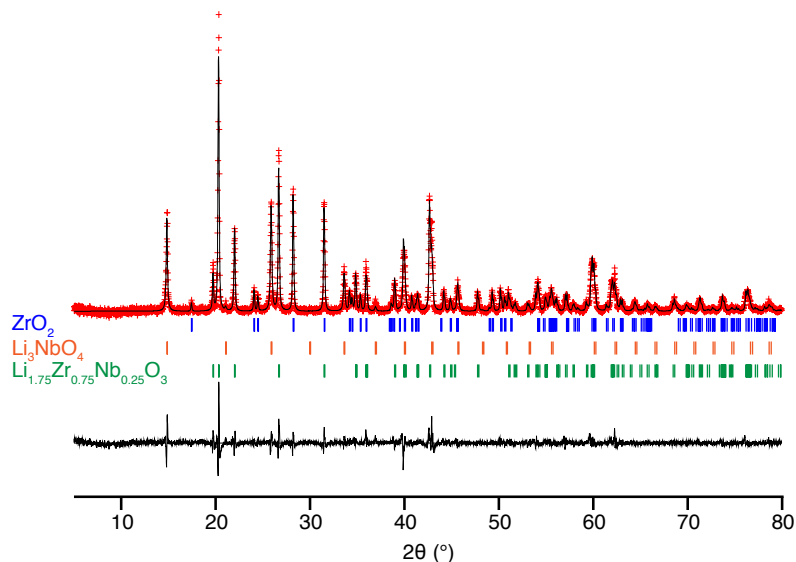


Figure 2: Indexed XRD diffractograms ($\lambda = 1.54056 \text{ \AA}$) and refinements for $\text{Li}_{1.75}\text{Zr}_{0.75}\text{Nb}_{0.25}\text{O}_3$. The experimental data points are shown in red, with the pattern obtained from the Rietveld refinements overlaid in black, and the difference curve below. The three phases indexed are $\text{Li}_{1.75}\text{Zr}_{0.75}\text{Nb}_{0.25}\text{O}_3$ (green), Li_3NbO_4 (orange) and ZrO_2 (blue).

In the case of Y-doped Li_2ZrO_3 , like the previous solid solutions, impurity phases were observed in the x-ray diffractograms of the $x = 0.05$ and 0.1 $\text{Li}_{2+x}\text{Zr}_{1-x}\text{Y}_x\text{O}_3$ samples (Figure 3), although they were unable to be indexed. A shift in reflections to lower angles with increasing Y doping denotes an increase in lattice parameters consistent with the substitution of the larger Y atom (ionic radii 0.9 \AA). Further details regarding the refined lattice parameters can be found in the Supporting Information.

Computational results

DFT calculations were performed to investigate the replacement of 25% of the Zr^{4+} ions with Nb^{5+} or Ta^{5+} ions in Li_2ZrO_3 along with the introduction of Li vacancies. The lowest energy doped configurations for Nb^{5+} and Ta^{5+} replacement (Figure 4) were 0.54 eV/Nb atom and 0.42 eV/Ta atom above the convex hull of the experimentally reported $\text{Li}^+-\text{Zr}^{4+}-(\text{Nb,Ta})^{5+}-\text{O}^{2-}$ phases. While these lowest energy configurations place the vacancy next to the dopant, the cell is too small to conclude that this configuration is the most stable in larger cells with doping levels much closer

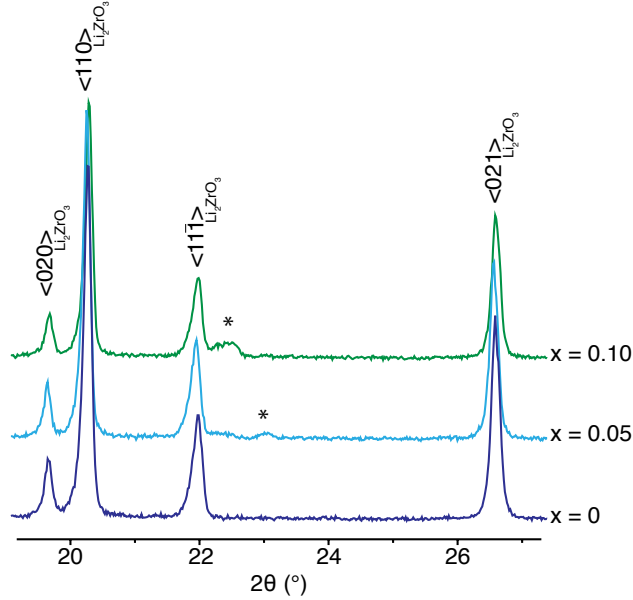


Figure 3: X-ray diffractograms ($\lambda = 1.54056 \text{ \AA}$) of $\text{Li}_{2+x}\text{Zr}_{1-x}\text{Y}_x\text{O}_3$, with $x = 0, 0.05$, and 0.1 . Reflections corresponding to the Li_2ZrO_3 phase are indexed as shown. Some very weak reflections (marked by asterisks) could not be indexed, and were assumed to arise from the presence of small amounts of impurity phases.

to those achieved experimentally. The energies of all the calculated configurations for the Nb and Ta doped systems relative to the energies of the corresponding binary oxides (Li_2O , Nb_2O_5 , Ta_2O_5 and ZrO_2) are shown in Figure 5.

For both Nb and Ta, the enthalpy of doping, ΔH_{dope} , is positive, showing that at 0 K the doped compositions are unstable relative to a combination of the parent compound Li_2ZrO_3 , ZrO_2 and $\text{Li}_3(\text{Nb,Ta})\text{O}_4$. This is in good agreement with the high fraction of impurity phases seen in the $x = 0.25$ experimental samples (Figure 1). The Ta doped compound has the lowest ΔH_{dope} , suggesting that it should be easier to introduce Ta than Nb into Li_2ZrO_3 . On this basis, Ta was chosen for an investigation of the doping enthalpy at a lower concentration of 3.125% replacement of Zr^{4+} ions in $2 \times 2 \times 2$ supercells. The lowest energy doped configuration at this concentration was only 0.02 eV/Ta atom above the convex hull, significantly lower than the 0.42 eV/Ta computed at the higher concentration (Figure S4). The repulsive interactions between doped Ta^{5+} ions will be much stronger at higher doping concentrations, where the average Ta^{5+} - Ta^{5+} separation is reduced,

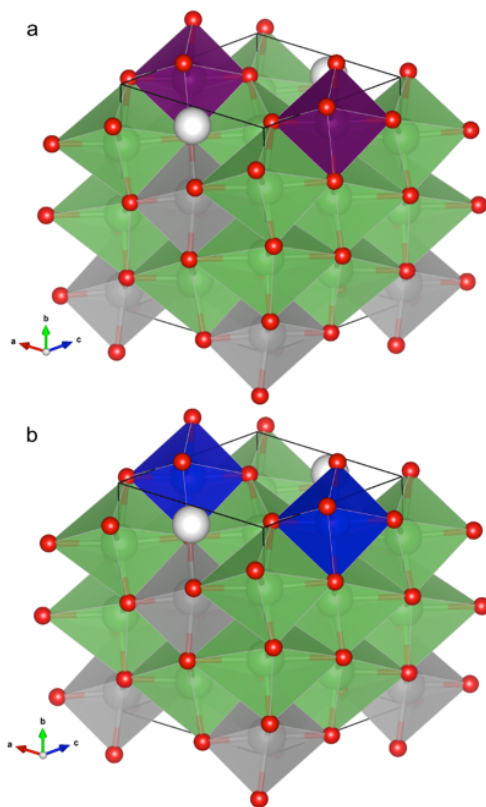


Figure 4: The lowest energy doping configurations computed for (a) Nb and (b) Ta in cells with composition $\text{Li}_7\text{Zr}_3(\text{Nb,Ta})\text{O}_{12}$. The coordination polyhedra of Li, Zr, Nb and Ta are shown in green, grey, purple and blue respectively, with O atoms in red. The vacant Li site is shown as a white sphere.

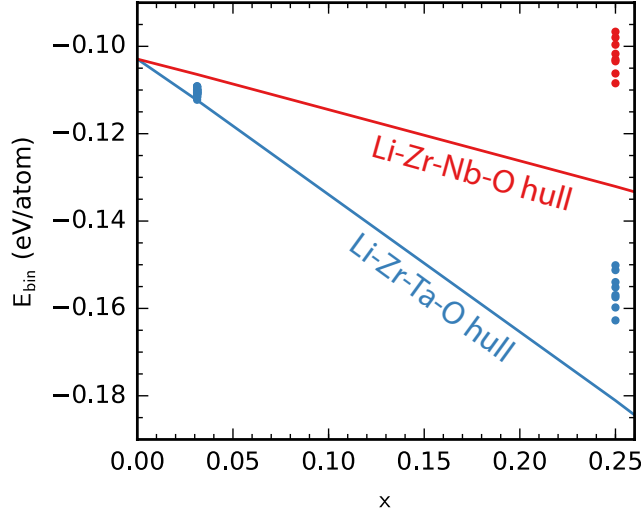


Figure 5: Energies of the DFT geometry-optimised configurations for $\text{Li}_{2-x}\text{Zr}_{1-x}\text{Nb}_x\text{O}_3$ ($x = 0.25$, purple markers) and $\text{Li}_{2-x}\text{Zr}_{1-x}\text{Ta}_x\text{O}_3$ ($x = 0.03125, 0.25$, blue markers), relative to the energies of the corresponding binary oxides Li_2O , ZrO_2 and Nb_2O_5 or Ta_2O_5 . The solid lines represent the convex hull for the systems, i.e. if a configuration lies on or below this line it is theoretically stable with respect to the other compositions in the Li-Ta-Zr-O (purple) or Li-Ta-Zr-O (blue) phase diagrams.

leading to a concentration dependent increase in the doping enthalpy per substituted Ta^{5+} ion.

Although the doped compounds are predicted to be unstable at 0 K even at low concentrations, configurational entropy due to the crystallographic disorder between Zr^{4+} and dopant ions, and Li^+ ions and vacancies, can stabilise doped compounds at finite temperatures. If full site disorder is included in the calculation of mixing entropy, then the doping free energies, ΔF_{dope}^1 , versus doping level, x , at the synthesis temperature of 1273 K are negative across the doping range up to $x = 0.25$, even taking the highest value of the doping enthalpy, with the doped compound more stable than the decomposition products (Figure 6). However, this is likely to be an upper limit on the estimation of stability. Comparison of the different possible calculated doping configurations shows that the energies of the most and least stable configurations differs by 0.6 eV/dopant atom for $\text{Li}_{2-x}\text{Zr}_{1-x}\text{Ta}_x\text{O}_3$ ($x = 1/32$), with no correlation seen between doping enthalpy and vacancy- Ta^{5+} separation (Figure S5). However, if we restrict the mixing entropy by assuming the positions of vacant Li sites are highly correlated to the positions of dopant atoms, as calculated in ΔF_{dope}^2 ,

this leads to a much smaller region of stability (Figure 6). In this case $\text{Li}_{2-x}\text{Zr}_{1-x}\text{Ta}_x\text{O}_3$ is predicted to be stable up to a doping limit of $x = 0.05$, and $\text{Li}_{2-x}\text{Zr}_{1-x}\text{Nb}_x\text{O}_3$ only up to $x = 0.01$. This small region of stability matches much better with the low limit of doping seen experimentally for these systems, indicating that entropy of mixing on the dopant site must be the dominant driving force for substitution, overcoming any enthalpic variance.

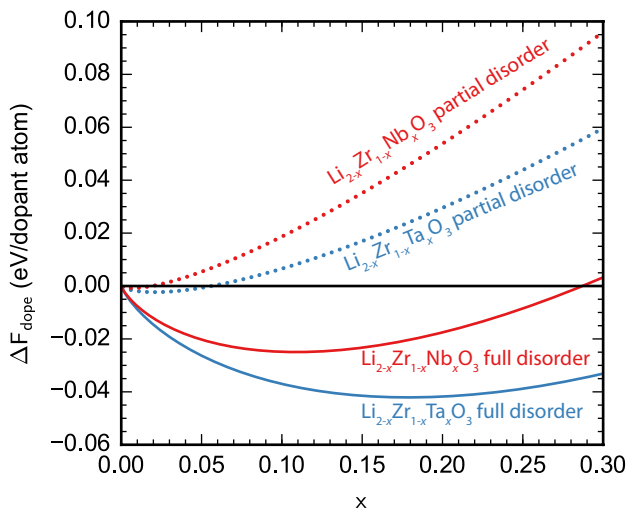


Figure 6: Doping free energies for Nb (purple) and Ta (blue) in $\text{Li}_{2-x}\text{Zr}_{1-x}(\text{Nb},\text{Ta})_x\text{O}_3$ as a function of doping level, x . Solid lines show the values of ΔF_{dope}^1 , for which full disorder is assumed over both the (Zr,Nb,Ta) and (Li,vacancy) sites. Dotted lines show the values of ΔF_{dope}^2 , for which it is assumed that the positions of vacant Li sites are highly correlated to the positions of dopant atoms, such that only disorder on the (Zr,Nb,Ta) contributes to mixing entropy. A negative value of the doping free energy represents thermodynamic stability of the doped compound against decomposition into competing phases.

^7Li NMR

For the purpose of determining the influence of dopants on the rate of Li ionic motion in the Li_2ZrO_3 structure, the $x = 0.05$ samples were subjected to a suite of variable-temperature ^7Li solid-state NMR experiments. From the XRD results, these samples are mostly phase pure within the parent Li_2ZrO_3 crystal structure, and therefore should provide a valid comparison to the motion observed in pure Li_2ZrO_3 .

The room-temperature ^7Li MAS NMR spectra for $\text{Li}_{1.95}\text{Zr}_{0.95}\text{Nb}_{0.05}\text{O}_3$, $\text{Li}_{1.95}\text{Zr}_{0.95}\text{Ta}_{0.05}\text{O}_3$ and $\text{Li}_{2.05}\text{Zr}_{0.95}\text{Y}_{0.05}\text{O}_3$ are shown in Figure 7, measured over the temperature range 295–773 K (spectra for undoped Li_2ZrO_3 are shown in the Supporting Information). The room temperature spectra for each sample are similar, showing an intense central transition (CT) resonance for this $I = 3/2$ quadrupolar nucleus at approximately 0 ppm, together with a spinning sideband manifold associated with the first-order quadrupolar-broadened satellite transitions (STs) extending over the range -200 to $+200$ ppm. While there are 2 distinct Li environments in the Li_2ZrO_3 structure, the small chemical shift range of ^7Li (~ 2 ppm) coupled with significant broadening due to ^7Li - ^7Li homonuclear dipole-dipole interactions means that the two similar environments cannot be resolved.

As the temperature is increased, the ST spinning sideband linewidth broadens (measured as full width at half maximum, FWHM), reaching a maximum at around 573 K for $\text{Li}_{1.95}\text{Zr}_{0.95}\text{Nb}_{0.05}\text{O}_3$ and $\text{Li}_{1.95}\text{Zr}_{0.95}\text{Ta}_{0.05}\text{O}_3$ and 673 K for $\text{Li}_{2.05}\text{Zr}_{0.95}\text{Y}_{0.05}\text{O}_3$ where they cannot be observed, before abruptly narrowing upon further heating (Figure 8). Changes in ST spinning sideband linewidth are a clear indication of ionic or molecular motion, as seen in other materials.^{15,48,49} In the case of the Li_2ZrO_3 structure, this corresponds to hopping of the Li ions between the two crystallographic sites, leading to initial broadening of the ST transitions, before narrowing at high temperatures when only a single averaged site is observed on the NMR timescale.¹⁹ Both the Nb and Ta doped materials behave quite similarly, while the Y doped material shows a similar broadening and then narrowing behaviour, but at a higher temperature. This is indicative of different rates of Li ionic mobility, and the following measurements aim to quantify this difference.

Quantitative information about the rates of ionic motion could be obtained from the determination of the spin-lattice relaxation times T_1 , which are sensitive to correlation times on the order of the Larmor frequency, that is $\sim 10^8$ Hz. Inverse T_1 times as a function of temperature are plotted in Figure 9. At higher temperatures there is an approximately linear correlation for all three doped samples, indicating Arrhenius behaviour and leading us to assume that the change in T_1 with temperature is due to changes in the ionic motion in the material occurring on the MHz scale.

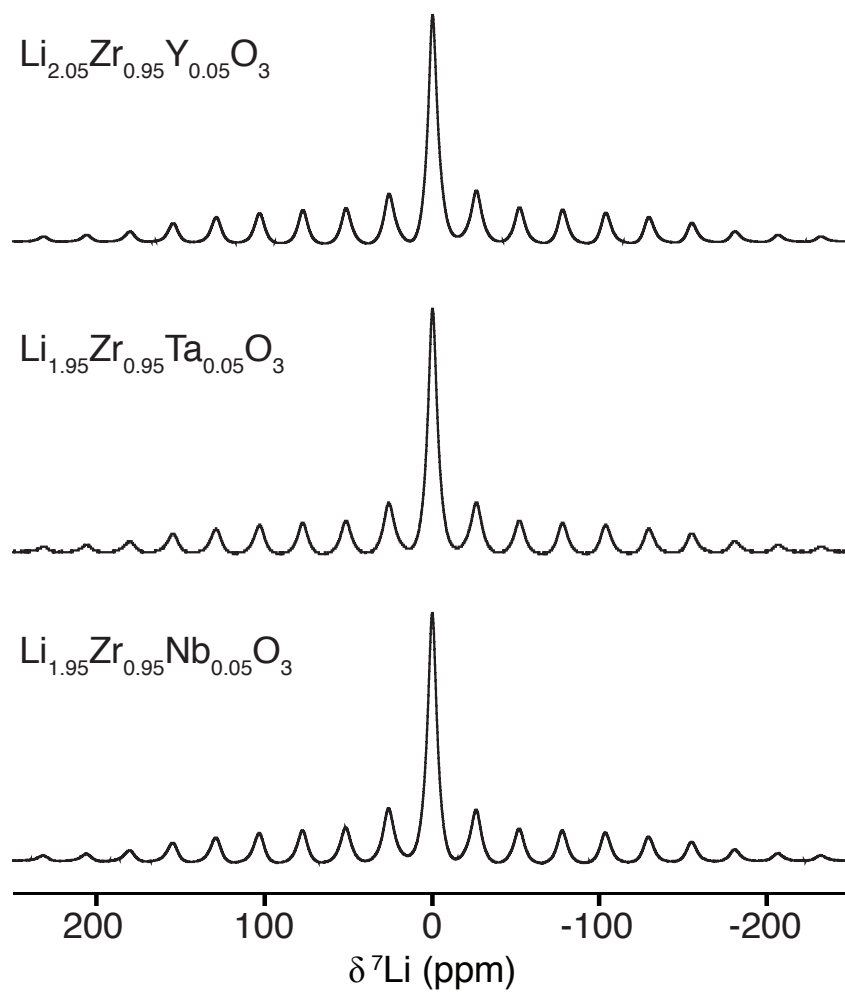


Figure 7: ${}^7\text{Li}$ MAS NMR spectra for $\text{Li}_{1.95}\text{Zr}_{0.95}\text{Nb}_{0.05}\text{O}_3$, $\text{Li}_{1.95}\text{Zr}_{0.95}\text{Ta}_{0.05}\text{O}_3$ and $\text{Li}_{2.05}\text{Zr}_{0.95}\text{Y}_{0.05}\text{O}_3$ measured at 295 K. All samples show a familiar pattern for a non-integer spin nucleus, with a sharp CT at ~ 0 ppm, and a set of spinning sidebands from the satellite transitions.

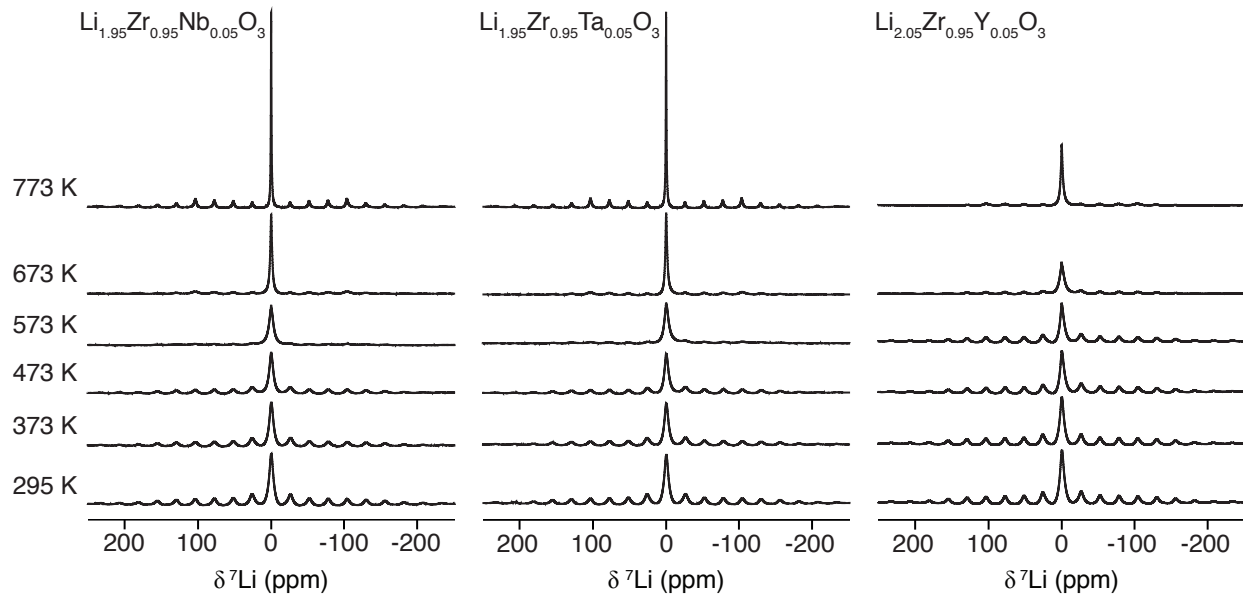


Figure 8: ${}^7\text{Li}$ MAS NMR spectra for $\text{Li}_{1.95}\text{Zr}_{0.95}\text{Nb}_{0.05}\text{O}_3$, $\text{Li}_{1.95}\text{Zr}_{0.95}\text{Ta}_{0.05}\text{O}_3$ and $\text{Li}_{2.05}\text{Zr}_{0.95}\text{Y}_{0.05}\text{O}_3$ measured from 295–773 K. The spectra were normalised between samples to the intensity at 295 K. For all the samples a similar behaviour is observed upon increasing temperature: a narrowing of the central transition linewidth and a broadening and subsequent narrowing of the satellite transition linewidths.

Additionally, the rapid increase in T_1^{-1} at higher temperatures indicates the possible existence of a diffusion-induced maximum value that was inaccessible within the experimental temperature range.

Thermogravimetric measurements

In order to investigate the effect of doping on the CO_2 absorption properties, both undoped Li_2ZrO_3 and the three doped samples ($x = 0.05$) were heated isothermally at 823 K for 60 h under flowing CO_2 . The resulting normalised mass curves are shown in Figure 10. All the doped samples showed lower levels of CO_2 absorption than pure Li_2ZrO_3 , with the Nb and Ta doped samples in particular showing somewhat surprisingly very minimal absorption.

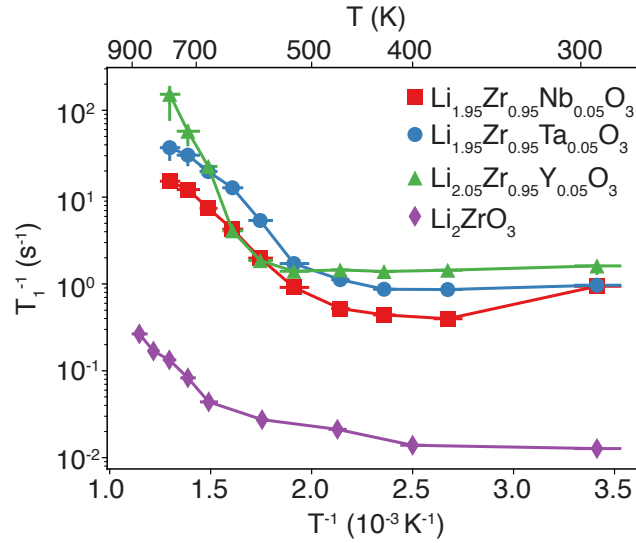


Figure 9: ${}^7\text{Li}$ relaxation rates T_1^{-1} as a function of inverse temperature for Li_2ZrO_3 , $\text{Li}_{2-x}\text{Zr}_{1-x}\text{Nb}_x\text{O}_3$, $\text{Li}_{2-x}\text{Zr}_{1-x}\text{Ta}_x\text{O}_3$ and $\text{Li}_{2+x}\text{Zr}_{1-x}\text{Y}_x\text{O}_3$. **Guidelines have been added to easily distinguish the trend in T_1^{-1} for the different samples.**

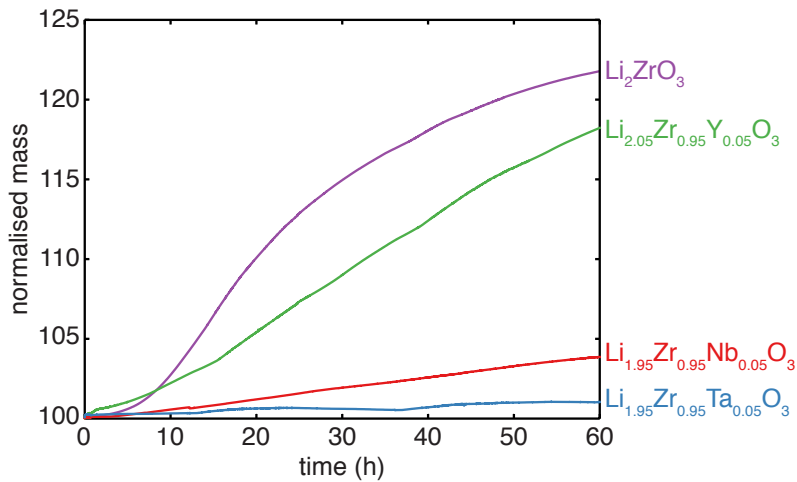


Figure 10: Normalised mass traces for both undoped Li_2ZrO_3 and the Nb, Ta and Y doped samples ($x = 0.05$), heated isothermally at 823 K for 60 h under CO_2 .

Discussion

In order to compare the rates of ionic mobility, and the activation energies of the conduction process in the three materials, we use a common parameter, the inverse correlation time τ_c^{-1} , that can be derived from the T_1 fitting using a relationship previously used in similar studies:^{50,51}

$$\frac{1}{T_1} = \frac{2\pi^2}{25} \cdot C_Q^2 \cdot \left(1 + \frac{\eta_Q^2}{3}\right) \cdot \left[\frac{\tau_c}{1 + \omega_0^2 \tau_c^2} + \frac{4\tau_c}{1 + 4\omega_0^2 \tau_c^2} \right] \quad (6)$$

where ω_0 is the ${}^7\text{Li}$ Larmor frequency ($\frac{\omega_0}{2\pi}({}^7\text{Li}) = 155.46$ MHz at 9.4 T), and values of the quadrupole coupling constant C_Q (99 kHz) and asymmetry parameter η_Q (0.17) were taken from the average experimentally determined values for pure Li_2ZrO_3 measured at room temperature. These values are similar to those from another recent NMR study of Li_2ZrO_3 ($C_Q = 86$ kHz, $\eta_Q = 0.08$) by Baklanova *et al.*¹⁹

If we take the τ_c^{-1} values to be equal to the average jump rates of their respective processes, τ^{-1} , we can fit the linear parts of each curve to **estimate** the activation energy E_A and pre-exponential factor τ_i^{-1} for the ionic motion using the Arrhenius relationship:⁵¹

$$\tau^{-1} = \tau_i^{-1} \cdot \exp\left(-\frac{E_A}{k_B T}\right) \quad (7)$$

The results from this fitting are shown in Figure 11 and Table 2. It should be noted that this activation energy is mainly sensitive to local motion in the materials, and does not account for self-correlated motion versus motion leading to long range diffusion. It is however a good estimate to compare the local ionic motion mechanisms that would contribute to bulk ionic conductivity.

Table 2: **Estimated** lithium ion activation energies E_A for the doped Li_2ZrO_3 samples as well as pure Li_2ZrO_3 determined from the ${}^7\text{Li}$ relaxation measurements from 523–873 K.

Sample	E_A (eV)
Li_2ZrO_3	0.43 ± 0.03
$\text{Li}_{1.95}\text{Zr}_{0.95}\text{Nb}_{0.05}\text{O}_3$	0.41 ± 0.01
$\text{Li}_{1.95}\text{Zr}_{0.95}\text{Ta}_{0.05}\text{O}_3$	0.44 ± 0.03
$\text{Li}_{2.05}\text{Zr}_{0.95}\text{Y}_{0.05}\text{O}_3$	0.91 ± 0.07

The dominant mechanism for lithium diffusion in pure Li_2ZrO_3 is considered to be direct hop-

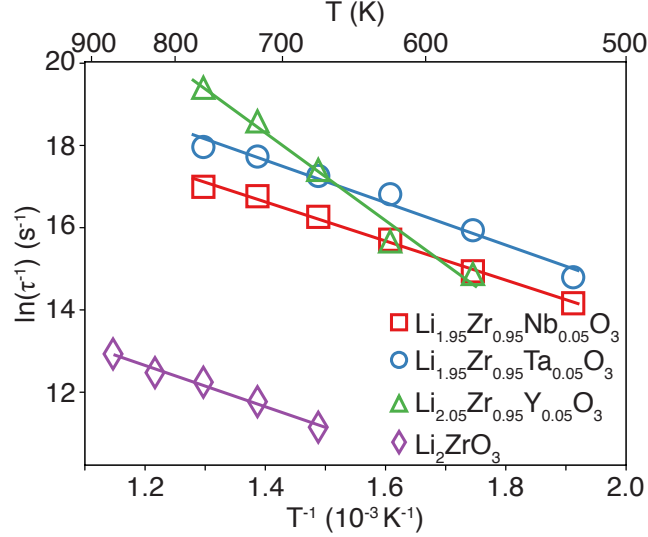


Figure 11: Arrhenius fitting of the inverse correlation times τ^{-1} , derived from the linear region of the ${}^7\text{Li}$ relaxation rates T_1 .

ping between crystallographic sites, requiring the presence of vacancies on both crystallographic sites. The origin for these vacancies, even in a nominally fully stoichiometric material, was suggested to result from the formation of a thin layer of a nonstoichiometric oxygen deficient phase at grain boundaries.^{52–54} Li_2O loss during synthesis may also result in Li and O vacancies. **There also may be small amounts of Nb and Ta impurities in the as-synthesised Li_2ZrO_3 (present in the ZrO_2 reagent) that would also lead to the formation of vacancies.**

The estimated activation energy of Li_2ZrO_3 from this study is lower than previously reported (0.64 eV) by Baklanova *et al.*,¹⁹ but is similar to the values found for both the Nb and Ta doped compounds. The doping produces lithium ion vacancies which enable hopping between nearby atomic sites, and the similar activation energy for the pure Li_2ZrO_3 is evidence that the same mechanism drives the lithium ionic motion in the undoped material as well. While the activation energy doesn't change upon doping, the overall conductivity likely increases due to the increase in the concentration of vacancies. Further measurements utilising impedance spectroscopy are planned to further characterise the influence of local structural changes on the overall bulk conductivity of the material.

The fact that the Y doped sample has a higher activation energy compared to the stoichiometric Li_2ZrO_3 indicates that the additional Li atoms present in the structure somehow impede the vacancy hopping mechanism. These additional Li atoms may also fill the vacancies formed at the grain boundaries or in the bulk, further decreasing the available vacancy concentration in the material and retarding the overall lithium mobility. Unfortunately, the limited stability range for vacancy doping confirmed from the first principles calculations means that it is not possible to synthesise compounds with higher concentrations of vacancies that might lead to more significant changes in the rates of ionic motion compared to pure Li_2ZrO_3 .

Further studies to improve our understanding of the formation of nonstoichiometric phases at grain boundaries will better elucidate the role they play in controlling ionic diffusion, as clearly this will also influence their effect on CO_2 absorption that also primarily occurs at surfaces and along grain boundaries. Investigating strategies to stabilise higher doped phases is also planned, in order to understand the connection between vacancy concentration and ionic diffusion.

Reviewing previous studies on Li_2CO_3 ,¹⁵ it was hypothesised that lower barriers to Li ionic motion lead to higher rates of CO_2 absorption, as there appeared to be a connection between the higher rates of Li ionic motion activated at higher temperatures that corresponded well with the temperatures at which more rapid absorption was seen. In the current work this theory is consistent with the slower absorption rate of the Y doped sample as compared to pure Li_2ZrO_3 observed in the TGA analysis, as the introduction of interstitial doping results in a higher activation energy barrier for Li motion. However, the converse behaviour is not observed for the Nb and Ta doped samples, which would be expected to display more rapid CO_2 absorption consistent with their **higher vacancy concentration** as compared to Li_2ZrO_3 .

One theory that would support our results is that Nb and Ta doping has a significant influence on the carbonation equilibria of Li_2ZrO_3 , decreasing the temperature required to regenerate the starting material. Considering the reaction in Equation (1), any modification that increases the stability of the Li_2ZrO_3 phase relative to Li_2CO_3 and ZrO_2 would cause the equilibrium to shift to the left, leading to a decrease in the amount of carbonated products formed. As discussed earlier,

when entropic effects are included the Nb and Ta doped samples are in fact found to be more stable than pure Li_2ZrO_3 (for small doping values), and therefore at the constant temperature at which the thermogravimetry in Figure 10 was performed, these doped samples would carbonate to a lesser extent relative to pure Li_2ZrO_3 . The equilibrium would only have to shift by 50–100 K to lead to this effect, which is reasonable given the doping free energy is on the order of ~ 0.05 eV (Figure 6). Unfortunately, the two factors of equilibrium and ionic mobility are not able to be maximised simultaneously: if the reaction is carried out at lower temperatures to shift the equilibrium back towards carbonation, then the ionic conduction is reduced and minimal carbonation is observed. A shift in equilibrium would also change the driving force for any ionic diffusion, which might also contribute to the slower than expected carbonation. This work therefore underlines the need to investigate doping schemes that can maximise gains in ionic dynamics while having careful control over the overall carbonation thermodynamics.

Conclusions

In this work we successfully synthesised various doped samples of Li_2ZrO_3 and used a combination of x-ray diffraction, theoretical calculations and solid state NMR to characterise their structure and rates of Li ionic mobility.

Vacancy doping with Nb and Ta was shown to lead to similarly lower energies of activation for Li motion as compared with interstitial doping with Y, and in the T_1 measurements these vacancy doped materials had **similar** activation energies **to** the pure Li_2ZrO_3 material. Unfortunately, all the doped samples displayed inferior CO_2 absorption behaviour to Li_2ZrO_3 , indicating that doping can also have a detrimental effect on the carbonation equilibria of the target material that works against the improvements in ionic conductivity created by the doping

This work shows the different strategies that can be used to characterise ionic motion in solid materials, and to quantify accurately the effect of different chemical doping methods. In particular, solid state NMR is a powerful technique in this respect, and shows promise to develop further our

understanding of the connection between structure, ionic motion and physical properties that are central to the development of novel CCS materials. It also underlines the balancing act that must be considered when developing new materials and doping schemes, aiming for significant changes in ionic conductivity without compromising the overall desired reaction thermodynamics.

Acknowledgements

The authors acknowledge funding from EPSRC Grant No. EP/K030132/1. M.T.D. acknowledges funding from the Cambridge Commonwealth Trusts and Trinity College, Cambridge, and thanks Clare College, Cambridge for the award of a Junior Research Fellowship. M.W.G. is grateful for support from the European Union's Horizon 2020 research and innovation programme under the Marie Skłodowska-Curie grant agreement No. 659764.

Data

All supporting data for this work can be found on <https://www.repository.cam.ac.uk>.

References

- (1) Pacala, S. *Science* **2004**, *305*, 968–972.
- (2) Hanak, D. P.; Anthony, E. J.; Manovic, V. *Energy Environ. Sci.* **2015**, *8*, 2199–2249.
- (3) Boot-Handford, M. E. et al. *Energy & Environmental Science* **2014**, *7*, 130.
- (4) Dean, C.; Blamey, J.; Florin, N.; Al-Jeboori, M.; Fennell, P. *Chemical Engineering Research and Design* **2011**, *89*, 836–855.
- (5) Abanades, J. C.; Alvarez, D. *Energy & Fuels* **2003**, *17*, 308–315.
- (6) Mosqueda, H. A.; Vazquez, C.; Bosch, P.; Pfeiffer, H. *Chemistry of Materials* **2006**, *18*, 2307–2310.

- (7) Ochs, D.; Brause, M.; Braun, B.; Maus-Friedrichs, W.; Kempter, V. *Surface Science* **1998**, *397*, 101–107.
- (8) Nakagawa, K. *Journal of The Electrochemical Society* **1998**, *145*, 1344.
- (9) Ida, J.; Xiong, R.; Lin, Y. *Separation and Purification Technology* **2004**, *36*, 41–51.
- (10) Pfeiffer, H.; Bosch, P. *Chemistry of Materials* **2005**, *17*, 1704–1710.
- (11) Kato, M.; Yoshikawa, S.; Nakagawa, K. *Journal of Materials Science Letters* **2002**, *21*, 485–487.
- (12) Avalos-Rendon, T.; Lara, V. H.; Pfeiffer, H. *Industrial & Engineering Chemistry Research* **2012**, *51*, 2622–2630.
- (13) Nair, B. N.; Burwood, R. P.; Goh, V. J.; Nakagawa, K.; Yamaguchi, T. *Progress In Materials Science* **2009**, *54*, 511–541.
- (14) Ida, J.; Lin, Y. *Environmental Science & Technology* **2003**, *37*, 1999–2004.
- (15) Dunstan, M. T.; Griffin, J. M.; Blanc, F.; Leskes, M.; Grey, C. P. *The Journal of Physical Chemistry C* **2015**, *119*, 24255–24264.
- (16) Avalos-Rendon, T.; Casa-Madrid, J.; Pfeiffer, H. *Journal of Physical Chemistry A* **2009**, *113*, 6919–6923.
- (17) Palacios-Romero, L. M.; Pfeiffer, H. *Chemistry Letters* **2008**, *37*, 862–863.
- (18) Palacios-Romero, L. M.; Lima, E.; Pfeiffer, H. *Journal of Physical Chemistry A* **2009**, *113*, 193–198.
- (19) Baklanova, Y. V.; Arapova, I. Y.; Buzlukov, A.; Gerashenko, A.; Verkhovskii, S.; Mikhalev, K.; Denisova, D.; Shein, I.; Maksimova, L. *Journal of Solid State Chemistry* **2013**, *208*, 43 – 49.

- (20) Ohashi, N. K., T. *Materials Research Society Symposium - Proceedings* **1999**, 547, 249–254.
- (21) Essaki, K.; Nakagawa, K.; Kato, M. *Nippon Seramikkusu Kyokai Gakujutsu Ronbunshi/Journal of the Ceramic Society of Japan* **2001**, 109, 829–833.
- (22) Veliz-Enriquez, M. Y.; Gonzalez, G.; Pfeiffer, H. *Journal of Solid State Chemistry* **2007**, 180, 2485–2492.
- (23) Xiong, R.; Ida, J.; Lin, Y. *Chemical Engineering Science* **2003**, 58, 4377–4385.
- (24) Pfeiffer, H.; Lima, E.; Bosch, P. *Chemistry of Materials* **2006**, 18, 2642–2647.
- (25) Pfeiffer, H.; Vazquez, C.; Lara, V. H.; Bosch, P. *Chemistry of Materials* **2007**, 19, 922–926.
- (26) Guzman-Velderrain, V.; Delgado-Vigil, D.; Collins-Martinez, V.; Lopez Ortiz, A. *Journal of New Materials For Electrochemical Systems* **2008**, 11, 131–136.
- (27) Kato, M.; Nakagawa, K.; Essaki, K.; Maezawa, Y.; Takeda, S.; Kogo, R.; Hagiwara, Y. *International Journal of Applied Ceramic Technology* **2005**, 2, 467–475.
- (28) Tranqui, D.; Shannon, R. D.; Chen, H.-Y.; Iijima, S.; Baur, W. H. *Acta Crystallographica Section B* **1979**, 35, 2479–2487.
- (29) Shannon, R. D.; Taylor, B. *US Patent No. 4042482* **1977**,
- (30) Hodeau, J.; Marezio, M.; Santoro, A.; Roth, R. *Journal of Solid State Chemistry* **1982**, 45, 170 – 179.
- (31) Enciso-Maldonado, L.; Dyer, M. S.; Jones, M. D.; Li, M.; Payne, J. L.; Pitcher, M. J.; Omir, M. K.; Claridge, J. B.; Blanc, F.; Rosseinsky, M. J. *Chemistry of Materials* **2015**, 27, 2074–2091.
- (32) Kresse, G. *Physical Review* **1996**, B54, 11169–11186.
- (33) Perdew, J. P.; Burke, K.; Ernzerhof, M. *Physical Review Letters* **1996**, 77, 3865–3868.

- (34) Kresse, G.; Joubert, D. *Phys. Rev. B* **1999**, *59*, 1758–1775.
- (35) FIZ Karlsruhe, G. ICSD Web.
- (36) Ong, S. P.; Richards, W. D.; Jain, A.; Hautier, G.; Kocher, M.; Cholia, S.; Gunter, D.; Chevrier, V. L.; Persson, K. A.; Ceder, G. *Computational Materials Science* **2013**, *68*, 314–319.
- (37) Taulelle, F.; Coutures, J.; Massiot, D.; Rifflet, J. *Bulletin of the International Society for Magnetic Resonance* **1989**, *11*, 318–320.
- (38) Ernst, H.; Freude, D.; Mildner, T.; Wolf, I. *Solid State Nuclear Magnetic Resonance* **1996**, *6*, 147–156.
- (39) Thurber, K. R.; Tycko, R. *Journal of Magnetic Resonance* **2009**, *196*, 84 – 87.
- (40) Dunstan, M. T.; Jain, A.; Liu, W.; Ong, S. P.; Liu, T.; Lee, J.; Persson, K. A.; Scott, S. A.; Dennis, J. S.; Grey, C. P. *Energy Environ. Sci.* **2016**, *9*, 1346–1360.
- (41) Barin, I. *Thermochemical Data of Pure Substances*; Wiley-VCH Verlag GmbH, 2008.
- (42) Ukei, K.; Suzuki, H.; Shishido, T.; Fukuda, T. *Acta Crystallographica Section C* **1994**, *50*, 655–656.
- (43) du Boulay, D.; Sakaguchi, A.; Suda, K.; Ishizawa, N. *Acta Crystallographica Section E* **2003**, *59*, i80–i82.
- (44) Smith, D. K.; Newkirk, W. *Acta Crystallographica* **1965**, *18*, 983–991.
- (45) Shannon, R. D. *Acta Crystallographica Section A* **1976**, *32*, 751–767.
- (46) Larson, A.; Dreele, R. V. General Structure Analysis System (GSAS). Los Alamos National Laboratory Report LAUR 86-748, 2000.
- (47) Toby, B. H. *Journal of Applied Crystallography* **2001**, *34*, 210–213.

- (48) Griffin, J. M.; Wimperis, S.; Berry, A. J.; Pickard, C. J.; Ashbrook, S. E. *The Journal of Physical Chemistry C* **2009**, *113*, 465–471.
- (49) Griffin, J. M.; Miller, A. J.; Berry, A. J.; Wimperis, S.; Ashbrook, S. E. *Physical Chemistry Chemical Physics* **2010**, *12*, 2989.
- (50) Abragam, A. *The principles of nuclear magnetism*; Oxford University Press: Oxford, 1998.
- (51) Indris, S.; Heitjans, P.; Uecker, R.; Roling, B. *The Journal of Physical Chemistry C* **2012**, *116*, 14243–14247.
- (52) Yamaguchi, K.; Suzuki, A.; Tonegawa, M.; Takahashi, Y.; Yasumoto, M.; Yamawaki, M. *Journal of the Mass Spectrometry Society of Japan* **1999**, *47*, 10–15.
- (53) Kawamura, Y.; Nishikawa, M.; Shiraishi, T.; Okuno, K. *Journal of Nuclear Materials* **1996**, *230*, 287 – 294.
- (54) Yamawaki, M.; Yamaguchi, K.; Suzuki, A. *Ionics* **2001**, *7*, 339–345.